

# Experimental and DFT Calculated IR Spectra of Guests in Zeolites: Acyclic Olefins and Host–Guest Interactions

Babgen Manookian, Eric D. Hernandez, Marcel D. Baer, Christopher J. Mundy, Friederike C. Jentoft,\* and Scott M. Auerbach\*

Cite This: *J. Phys. Chem. C* 2020, 124, 10561–10572

Read Online

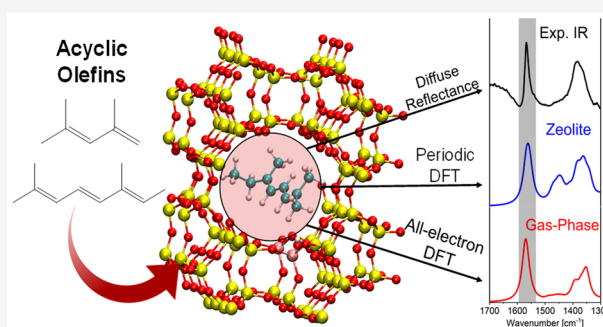
ACCESS |

Metrics & More

Article Recommendations

Supporting Information

**ABSTRACT:** We performed experimental and periodic density functional theory (DFT) IR spectroscopy to investigate the adsorption of acyclic olefins over both acidic and nonacidic zeolites. Two conjugated polyenes, 2,4-dimethyl-1,3-pentadiene (I) and 2,6-dimethyl-2,4,6-octatriene (II) were studied to probe organic intermediates that can be formed during methanol conversion and lead to deactivating species known collectively as “coke.” We computed vibrational spectra using zeolite-adsorbed and gas-phase models for both neutral and protonated forms of I and II and compared these DFT results to diffuse reflectance IR Fourier transform (DRIFT) spectra of zeolite–guest systems. Our experimental and computational results are precise enough to pinpoint the surprising fact that the gauche *s*-cis conformation of species I is the major conformer during adsorption over dealuminated zeolite  $\beta$ . Computed zeolite-adsorbed spectra of the protonated species I and II best represent the DRIFT spectra obtained after the adsorption of the olefins on HMOR at 20 °C, with computed bands at 1543 and 1562  $\text{cm}^{-1}$  for molecules I<sup>+</sup> and II<sup>+</sup>, respectively, attributed to the allylic stretching mode,  $\nu(\text{C}=\text{C}-\text{C}^+)$ . These computed band frequencies are within 6  $\text{cm}^{-1}$  of experimental data and confirm that the interaction between neutral acyclic olefins and acidic zeolites leads to protonation of the olefin. A comparison of computed spectra of the protonated species in the gas phase to those in the zeolite indicates that the electrostatic interaction between alkenyl and alkadienyl cations and negative zeolite framework does not significantly impact the position of the allylic stretching bands. These results highlight that computed spectroscopy and thermodynamics coupled with experimental spectra can be used to elucidate complex mixtures in zeolites, and certain spectral features of adsorbed olefins can be accurately modeled by gas-phase calculations.



## 1. INTRODUCTION

Acidic zeolites are microporous solids that are used as acid catalysts for a variety of chemical processes of industrial relevance, including various hydrocarbon transformations and the conversion of methanol to fuels and other value-added products.<sup>1–3</sup> During methanol or hydrocarbon conversions, these catalysts suffer from deactivation through the formation of carbonaceous byproducts known collectively as “coke”.<sup>4–6</sup> Understanding the mechanisms by which coke species form is of paramount importance to minimize catalyst deactivation and maximize catalyst lifetime and product formation.<sup>7,8</sup> In situ IR spectroscopy is a powerful technique for investigating the nature of intermediates that lead to coke and other products during zeolites catalysis.<sup>9–11</sup> The integration of experiments and predictive computations of IR spectra of zeolite–guest systems can be critical for assigning spectra of complex, reactive assemblies.<sup>12</sup> As periodic density functional theory (DFT) calculations have become more routine, methodological questions arise about the appropriate and efficient computational treatment of host–guest vibrational cou-

plings,<sup>13</sup> and thermal fluctuations of zeolite–guest systems at finite temperatures. Physical questions arise about the nature of adsorbed guests and the influence of specific host–guest interactions on the IR spectra.<sup>11</sup> In the present work, we combine IR spectroscopy experiments with periodic DFT of olefins adsorbed on acidic and nonacidic zeolites to investigate how the interaction between the zeolite framework and adsorbed olefins influences the vibrational spectra, and how predictive calculations can efficiently capture these effects.

The mechanisms by which hydrocarbons transform within acidic zeolites can be quite complex and may involve long-lived organic surface species, in some instances referred to as the “hydrocarbon pool.”<sup>14</sup> The various chemical species in

Received: February 12, 2020

Revised: April 10, 2020

Published: April 23, 2020



hydrocarbon pools are thought to play active roles<sup>1,15</sup> in some catalytic processes but can also transform to coke—thereby deactivating a given catalyst.<sup>8,16</sup> The identification of precursors in a hydrocarbon pool by IR spectroscopy poses a challenge because of the complexity of coexisting molecules, possibly overlapping IR bands, and limited knowledge of the influence of zeolite–guest interactions on IR spectral shifts.<sup>11</sup> One way to address this problem is to use hypothesized molecular proxies to pinpoint spectral features associated with a subset of chemical moieties, which in turn can be used to identify the makeup of a complex mixture such as the hydrocarbon pool. Acyclic dienes and trienes serve as useful model compounds, because they are the conjugate bases of species reported to exist in the hydrocarbon pool and can interact with the acidic zeolite framework generating cyclic conjugated species that proceed to either desired products or coke.<sup>17</sup> Below, we measure and simulate IR spectra of olefins I and II (Figure 1) in acidic HMOR zeolite and in nonacidic dealuminated zeolite  $\beta$  to determine and assign unambiguous spectral fingerprints of these important species upon adsorption in zeolites.

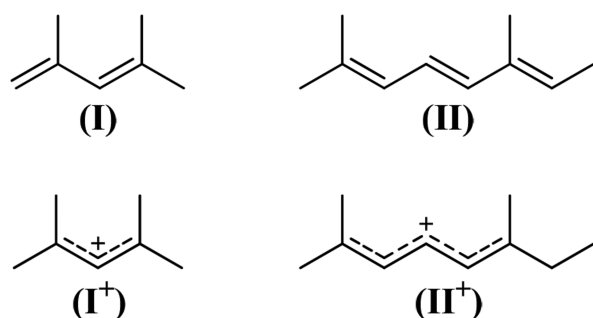


**Figure 1.** (I) 2,4-Dimethyl-1,3-pentadiene and (II) 2,6-dimethyl-2,4,6-octatriene are the two acyclic olefins used for this work. The protonated forms are denoted as I<sup>+</sup> and II<sup>+</sup>.

The adsorbed state of the guest molecules in zeolite pores can be monitored using experimental IR techniques.<sup>18,19</sup> Vibrational bands associated with guest species can be used as spectral fingerprints to determine catalytic properties such as the preferential adsorption of specific molecules<sup>19</sup> and the loading capacities.<sup>18</sup> However, the presence of complex mixtures in zeolites can produce spectral congestion, which can obfuscate the analysis of adsorbed states.<sup>19</sup> In such cases, computational spectroscopy serves as a powerful tool with the ability to obtain IR spectra of single molecules, and thus decrease the ambiguity in band assignments. We exploit this idea by obtaining DFT-computed IR spectra for single molecules and using those data to determine if those molecules are present in the experiment by comparison with experimental spectra.

Several computational methods are available for the calculation of IR spectra of condensed-phase systems, including normal-mode analysis (NMA) and correlation-function analysis via molecular dynamics (MD), each with its advantages and disadvantages.<sup>20</sup> By invoking the harmonic oscillator approximation, NMA provides a direct model of IR spectra with band assignments provided by the normal mode coordinates, requiring the calculation and diagonalization of the force constant matrix of second derivatives at optimized geometries.<sup>13</sup> For example, Hemolsoet and co-workers used

NMA to study the 100 cm<sup>-1</sup> red shift of OH stretching frequencies for ethanol and methanol when adsorbed on zeolites HZSM-5 and HSAPO-34.<sup>21</sup> In contrast, one can obtain IR spectra at finite temperatures, and beyond the harmonic approximation, by Fourier transforming the dipole autocorrelation function computed by MD.<sup>22</sup> We note that the MD approach to IR spectra does not necessarily allow for easy assignments of IR bands and can be quite computationally demanding when ab initio MD is required.<sup>20</sup> In the present work, we computed IR spectra of olefin–zeolite systems using NMA because of its computational efficiency, ease of making band assignments, and direct comparability with gas-phase NMA calculations. Within the NMA approach, we modeled finite temperature effects on IR spectra efficiently by averaging spectra for different snapshots from ab initio MD, as described in **Methods**.

The measured and computed IR spectra reported below demonstrate that adsorption of I on nonacidic zeolite  $\beta$  leads to a conformational mixture that contains mostly the lower-energy gauche *s-cis* conformer. The data below support the notion that protonation readily occurs upon adsorption of neutral acyclic olefins I and II in HMOR zeolite at 20 °C. Remarkably, the experimental and computational results also suggest that for certain spectroscopic features, such as allylic stretching bands, understanding the vibrational spectra of alkenyl and alkadienyl cations in acidic zeolites requires only taking into account the relevant state of the *gas-phase species*.

The remainder of this paper is organized as follows: in **Methods**, we describe the experimental and computational techniques used for obtaining vibrational spectra of acyclic olefins; in **Results and Discussion**, we discuss the resulting IR spectra with a focus on determining the nature of the adsorbed species and the interactions between guest molecules and nonacidic and acidic hosts. Finally, in **Conclusions**, we summarize the article and offer concluding remarks on the impact of this work.

## 2. METHODS

**2.1. Experimental Methods.** Here, we explain the rationale behind the design of our experimental study, followed by details on zeolite preparation and characterization methods as well as IR spectroscopy approaches.

Host–guest interactions in acidic zeolite catalysts involve both confinement in nanopores as well as specific interactions with Brønsted acid sites. We have investigated these two contributions separately by studying the IR spectra of acyclic olefins in comparable dealuminated and Brønsted-acidic zeolites. For the Brønsted-acidic zeolite, we have chosen acidic mordenite (HMOR) because of its general importance in zeolite catalysis<sup>23</sup> and its relatively large pores allowing sorption by a range of acyclic and cyclic species of interest. In principle, using dealuminated MOR would make comparisons of results with HMOR the most straightforward. In practice, however, we have found (as have others<sup>24,25</sup>) that dealuminating MOR-type zeolites causes their crystal structure to partially collapse. In contrast, we have found that dealumination of BEA-type zeolites leaves their crystal structure intact (details on X-ray diffraction (XRD) data discussed below). Although the framework structures of zeolite types BEA and MOR are different in detail, they are also quite similar in that they both contain 12-ring channels that can hold spheres with a diameter as large as 6.7 Å,<sup>26</sup> thus providing very similar nanopore environments. As such, we have performed

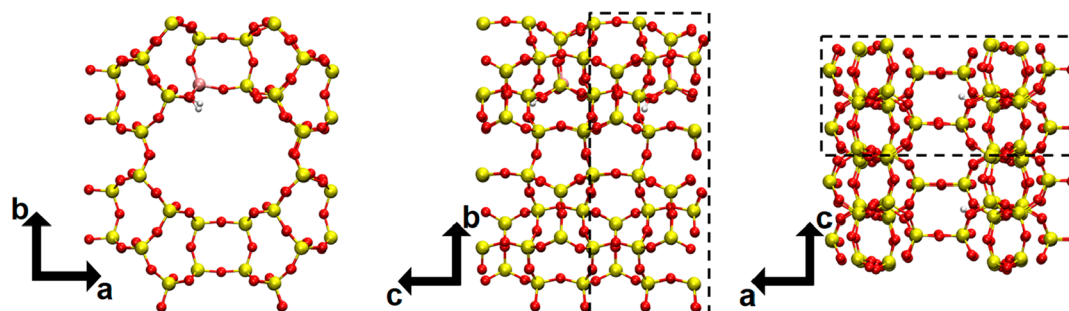


**Figure 2.** Illustration of the HMOR supercell used for periodic DFT calculations. Along the *c*-direction, an extra unit cell was included to create the  $1 \times 1 \times 2$  supercell that limits interaction of guest molecules in neighboring periodic images. The HMOR unit cell is highlighted by the dashed box.

zeolite–guest IR experiments using dealuminated BEA (deAl-BEA) for comparison with those using HMOR, to disentangle nanopore confinement effects from interactions with Brønsted acid sites.

Mordenite (MOR, Si/Al = 10) and zeolite  $\beta$  (BEA, Si/Al = 12.5) were obtained in the ammonium ion ( $\text{NH}_4^+$ ) form from Zeolyst International.  $\text{NH}_4^+$ -form zeolites were calcined in a horizontal tube furnace at a temperature of 500 °C for 2 h under a flow of 100 mL  $\text{min}^{-1}$  synthetic dry air (Airgas, 99.999%), driving off ammonia ( $\text{NH}_3$ ) and yielding the acidic forms, HMOR and HBEA. Dealumination of zeolites MOR and BEA was performed by treating the  $\text{NH}_4^+$ -form of each zeolite with 70 wt % nitric acid at 80 °C. The resulting sample was washed with deionized water and then dried at room temperature for several hours prior to calcination at 500 °C. Figure S1 in Supporting Information shows the powder XRD patterns for both zeolites before and after this dealumination process. Figure S1 clearly shows that while deAl-BEA retains its crystal structure, deAl-MOR loses substantial XRD intensity at several reflections, notably at  $2\theta$  values in the range 19–32°. These results regarding the partial collapse of MOR upon acid dealumination and the retention of BEA crystal structure during the same process are consistent with prior studies reported by O'Donovan et al.<sup>24</sup> and Müller et al.<sup>25</sup> as detailed in the Supporting Information.

DRIFT spectra (32 scans, 4  $\text{cm}^{-1}$  resolution) were collected using a PerkinElmer Spectrum 100 FTIR equipped with MCT detector. In situ DRIFTS experiments were performed in a Harrick high temperature reaction chamber fitted with ZnSe windows and situated within a Harrick Praying Mantis diffuse reflectance accessory. Calcined zeolites were diluted in KBr (1Zeolite:2KBr by mass), activated in situ at 400 °C for 0.5 h under a flow of 30 mL  $\text{min}^{-1}$  dry air, and then purged with  $\text{N}_2$  (Airgas, 99.999%). Following activation, the zeolite was cooled to 20 °C and either I or II was introduced into the reaction chamber via 1  $\mu\text{L}$  syringe pulses. A spectrum of KBr, dehydrated in situ, was used as a background. Difference spectra were calculated by subtracting the Kubelka–Munk spectrum of the activated zeolite from the Kubelka–Munk spectrum of the zeolite with adsorbate.

Brønsted and Lewis acid site concentrations within the deAl-BEA zeolite sample were determined by FTIR spectroscopy of adsorbed pyridine (Acros, 99.9%). A detailed description of the characterization by pyridine–FTIR is given in the Supporting Information (see Figure S2). Adsorption of pyridine on deAl-BEA at 150 °C and subsequent outgassing revealed that the sample does not exhibit any measurable quantity of Brønsted or Lewis acid sites after dealumination. As such, both the XRD and FTIR results for deAl-BEA indicate

that this zeolite sample serves our purpose of providing a suitable material, with ordered channels of size 6.7 Å and without measurable acidity, for comparison with HMOR.

**2.2. Computational Methods.** **2.2.1. Modeling the Zeolite.** The unit cell for calcined MOR was obtained from the Structure Commission of The International Zeolite Association,<sup>26,27</sup> and the T4 crystallographic site was substituted with an Al atom resulting in a negative charge which was compensated by a proton. The T4 site is located along the 12-membered-ring straight channel of MOR and exhibits high activity and easy accessibility.<sup>28,29</sup> Previously optimized<sup>30</sup> unit cell parameters for HMOR [ $a = 18.323$  Å,  $b = 20.795$  Å,  $c = 7.626$  Å,  $\alpha = \beta = \gamma = 90^\circ$ ] were used and agree well with experimental data<sup>31</sup> ( $a = 18.094$  Å,  $b = 20.516$  Å,  $c = 7.542$  Å,  $\alpha = \beta = \gamma = 90^\circ$ ). To avoid interaction between guest molecules in adjacent cells, we expanded the unit cell in the *c*-direction creating a  $1 \times 1 \times 2$  supercell (Figure 2) with the formula  $\text{H}_2\text{Al}_2\text{Si}_{94}\text{O}_{192}$  (Si/Al ratio of 47) to be used in all acidic zeolite calculations. A similar approach was used for the nonacidic case, where, in contrast, no Al atoms were incorporated in the super cell ( $\text{Si}_{96}\text{O}_{192}$ ).

**2.2.2. Electronic Structure Calculations.** We used CP2K<sup>32</sup> for periodic DFT of zeolite–guest and isolated neutral guest systems, allowing geometry optimization, normal-mode analysis (NMA) with convenient visualization of normal modes, and ab initio molecular dynamics to model IR spectra at finite temperatures. We used periodic DFT within the generalized gradient approximation with the BLYP exchange–correlation functional as implemented in CP2K.<sup>32</sup> The commonly used hybrid functional, B3LYP, is not available within CP2K and therefore limited us to the BLYP functional. However, based on our results, as well as those previously reported in the literature,<sup>20,33</sup> the BLYP functional provides adequate frequencies for qualitative, and in many cases, quantitative comparisons with experimental spectra. Corrections by Grimme et al. (DFT-D3) are used to take into account dispersion forces and obtain more accurate energetics.<sup>34</sup> For core electrons, Goedecker–Teter–Hutter norm-conserving pseudopotentials optimized for the BLYP functional are used,<sup>35</sup> while the valence electron wave functions are expanded in terms of a triple- $\zeta$  valence polarized basis set (TZVP) comparable to 6-311G(d).<sup>36</sup> Within the CP2K scheme,<sup>32</sup> the electron density is described using an auxiliary plane-wave basis set with a 400 Ry cutoff.

Gas-phase protonated species were modeled using the Gaussian 09 software package.<sup>37</sup> Calculations were performed using the BLYP functional via DFT and a 6-311G(d) basis set to describe the core and valence electrons, thus allowing for appropriate comparisons between gas-phase and zeolite-

adsorbed states via computational results from Gaussian and CP2K.

**2.2.3. Dynamics.** Computed IR spectra of guest molecules **I** and **II** in HMOR zeolite were obtained using two different models: full optimization or ensemble average. Both models are described below.

For the full optimization model, either guest was placed inside the pore of HMOR near the Brønsted acid site. A full geometry optimization (zeolite and guest) was then conducted followed by NMA. We ran test calculations where we included in NMA successively more zeolite atoms close to guest **II**<sup>+</sup> [within a radius of  $\delta(\text{Å})$ ], all the way up to including the full HMOR zeolite. Figure S3 in the Supporting Information shows the resulting spectra in the IR region of interest (1300–1700  $\text{cm}^{-1}$ ), indicating that including zeolite atoms has no effect on the positions of the bands in this region; however, there does appear to be a progressive increase in the overall intensity with inclusion of more framework atoms. As such, we included only the guest atoms in NMA for computing IR spectra. All frequencies were scaled using the vibrational scaling factor for BLYP/6-311G(d) of 0.998, reported in the NIST online database.<sup>38</sup> The resulting frequencies and intensities from NMA were incorporated into Lorentzian functions with a full width at half-maximum (fwhm) of 15  $\text{cm}^{-1}$ , as we have done in our previous spectroscopic simulations,<sup>22,39</sup> to simulate IR spectra within the full optimization model.

For the ensemble average model, we performed ab initio molecular dynamics (AIMD) of each zeolite–guest system at experimentally relevant temperatures ( $T = 20, 130, 200\text{ °C}$ ) to test whether thermal fluctuations influence IR spectra of these zeolite–guest systems. Each system was initialized with a guest molecule in the supercell at the active site. AIMD was then performed for 8–9 ps using a 0.5 fs time step and a Nosé–Hoover chain thermostat with a frequency of 1000  $\text{cm}^{-1}$ . Next, 30 snapshots of the system were extracted at random from the latter 6–7 ps of each AIMD simulation. For each image, we geometry-optimized the guest while keeping the zeolite framework fixed. Such an approach conserves the thermal fluctuations of the zeolite while keeping the resulting normal-mode frequencies real; otherwise, each snapshot can produce different numbers of vibrational modes. NMA was then performed on the guest, once again omitting the zeolite atoms, and the resulting (scaled) frequencies and intensities were incorporated into Lorentzian functions with a fwhm of 15  $\text{cm}^{-1}$  to yield a simulated spectrum for each snapshot. Finally, all 30 spectra were averaged to provide the ensemble-averaged spectrum for the guest at a desired experimental temperature.

To investigate the thermodynamics of guest and zeolite–guest systems within the periodic DFT scheme, we computed Helmholtz free energies in the NVT ensemble via NMA within a multidimensional harmonic oscillator model using the formula shown in Supporting Information, Figure S4. The harmonic frequencies were obtained from NMA after full optimization to compute the change in free energy between neutral and protonated states of each acyclic olefin. We also used these free energies to analyze stabilities of various conformers of **I**, **II**, **I**<sup>+</sup>, and **II**<sup>+</sup> as described in detail below.

An investigation of the impact of zeolite–guest interactions on spectral features of protonated guests requires the calculation of IR spectra in the gas phase, for comparison. Periodic boundary conditions require a net charge of zero in a given cell. Thus, to model isolated, protonated guests, we employed Gaussian 09 software to obtain spectra of isolated **I**<sup>+</sup>

and **II**<sup>+</sup>. For each gas-phase species considered, we carried out a full geometry optimization followed by NMA to obtain vibrational frequencies and intensities. Gas-phase calculations were performed using the BLYP/6-311G(d) model chemistry as implemented in Gaussian 09,<sup>37</sup> for consistency with the BLYP/TZVP treatment within CP2K for zeolite–guest systems. The resulting BLYP/6-311G(d) frequencies were scaled and incorporated into Lorentzian functions with a fwhm of 15  $\text{cm}^{-1}$  to obtain a computed IR spectrum.

**2.2.4. Conformational Analyses.** Each of the species **I**, **II**, and **II**<sup>+</sup> exhibits a rich array of conformational states. (Species **I**<sup>+</sup> exhibits only a single conformer.) We modeled this conformational space to investigate whether mixtures of conformers are present or whether a single conformer predominates. To address this issue, we computed relative free energies and IR spectra of all relevant conformers in gas-phase and zeolite-adsorbed states. We used these free energies to Boltzmann-weight the single-conformer IR spectra and yield a conformationally averaged IR spectrum for comparison with experimental IR data. We also utilized techniques to compute the barriers between relevant conformational states for olefin **I**. Within the CP2K scheme, we employed the climbing nudged elastic band method with seven replicas to obtain transition states and corresponding free energies of activation.

### 3. RESULTS AND DISCUSSION

In this section, we discuss our findings regarding the use of experimental and computational IR spectra to elucidate the nature of adsorbed acyclic olefins. First, we consider the conformational state of olefin **I** in nonacidic dealuminated  $\beta$  zeolite (deAl-BEA) using computed thermodynamics and comparison of computed spectra with experiment. Second, we investigate how the adsorption of guests **I** and **II** in (acidic) HMOR affects the corresponding IR spectra. Finally, we analyze the nature of electrostatic interactions between a negatively charged framework  $\text{MOR}^-$  and adsorbed cations **I**<sup>+</sup> and **II**<sup>+</sup>, as probed through the corresponding IR spectra.

**3.1. Adsorption of 2,4-Dimethyl-1,3-pentadiene on a Nonacidic Host: Contributions of Rotational Conformers to IR Spectrum.** We begin by using IR spectroscopy to determine the nature of molecule **I** adsorbed on nonacidic, large-pore zeolites. We are interested in the adsorption in all-silica zeolites because it provides data on a baseline level of confinement without acid sites for comparison with results in Section 3.2, which contains acid sites. We have carried out experimental IR measurements of **I** over deAl-BEA. As discussed above in Methods, we model the pore space of deAl-BEA by using DFT to compute properties of molecule **I** in all-silica MOR, which contains channels very similar in size to those of BEA. Regarding guest species **I**, it has been reported that molecules of this nature exist in either *s*-cis or *s*-trans conformations,<sup>40,41</sup> prompting us to begin by investigating the equilibrium between the two conformers using computed Gibbs and Helmholtz energies, and the impact of these conformers on the IR spectra.

Dienes such as molecule **I** have a dihedral angle along the single bond in between the two C=C bonds, resulting in two stable conformations denoted as *s*-trans and *s*-cis, where the ‘*s*’ indicates torsion around the single bond. Previous reports on substituted dienes suggest that the *s*-trans conformer can be lower in energy by as much as 3 kcal/mol, thus exhibiting higher population at thermal equilibrium.<sup>40,41</sup> We investigated the thermodynamic stabilities of conformers of **I** by computing

free energy profiles for the *s*-cis and *s*-trans conformers in vacuum and over all-silica MOR (Table S1 in Supporting Information). Interestingly, we found that a *gauche s*-cis conformation of I has lower free energies than its *s*-trans counterpart at 20 °C. We found the *gauche s*-cis (with a dihedral angle of  $-44^\circ$ ) to be lower in Helmholtz free energy by 0.27 kcal/mol in all-silica MOR. In vacuum, we found a similar trend where the *gauche s*-cis is lower in Helmholtz free energy by 0.26 kcal/mol (Table S1). We found from visual inspection of the highest-occupied molecular orbitals (HOMOs in Figure 3) that the surprising stability of the

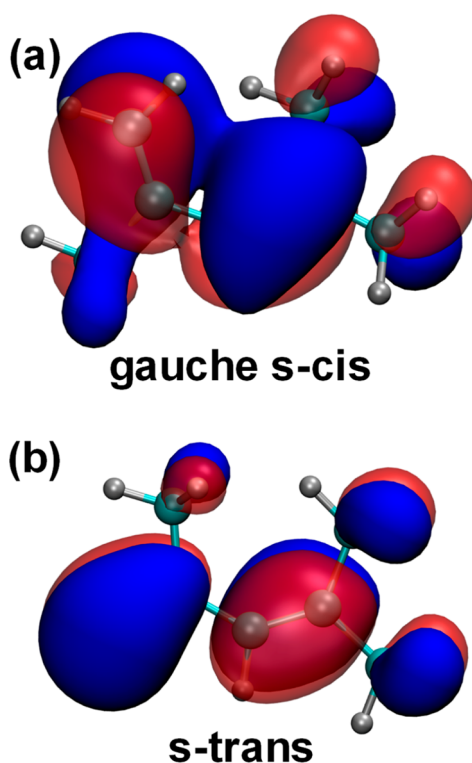


**Figure 3.** Highest occupied molecular orbitals (HOMOs) of rotational conformers for olefin I computed in the gas-phase, where the red/blue denotes the phase (sign) of the HOMO. Extended region of conjugated electron density involving neighboring methyl group, shown in blue, lowers energy for (a) *gauche s*-cis conformer relative to (b) *s*-trans conformer.

*gauche s*-cis conformation arises from electron delocalization between  $\pi$ -bonds and nearby methyl groups, which is possible only in the *gauche s*-cis conformation. In particular, Figure 3 shows the phase (i.e., sign) of the HOMO in red/blue. In the *s*-trans conformation, the HOMO of the conjugated diene exhibits a nodal plane between the two  $\pi$ -bonded regions, represented by the change in color within the orbital. However, at a dihedral angle of  $-44^\circ$ , the *gauche s*-cis conformation is stabilized by an extended region of conjugated electron density shown in blue, involving the  $\pi$ -system and the neighboring methyl group. Such extended conjugation appears impossible in the *s*-trans conformer.

To determine whether IR spectra are expected to exhibit an equilibrium distribution of conformers of species I, we computed the rotational activation free energies for vacuum and zeolite-adsorbed (all-silica MOR) conformational transitions. Such barriers help to determine whether conformational transitions and equilibrium are likely under experimental

conditions of temperature and observation time. We carried out these calculations by employing a climbing-image nudged elastic band technique with seven images. Figure S5 shows the free energy profile for rotation of species I along its C–C single bond in all-silica MOR. We also computed rotational barriers for I in the gas phase with other, more accurate model chemistries and found qualitatively similar results to those in Figure S5 (see Table S1). Notably, the barrier for rotation in MOR of 3.85 kcal/mol is higher than the vacuum value of 1.46 kcal/mol, most likely due to steric hindrance inside the MOR channel. Barriers of these magnitudes at 20 °C suggest rotational time scales of no more than 100 ps, indicating sufficiently rapid conformational transitions to produce an equilibrium distribution in the zeolite. For this reason, we computed IR spectra for each stable conformer separately and averaged them with Boltzmann weighting for comparison with experimental DRIFTS data, as discussed below.

Our effort to interpret IR spectra and investigate the effects of a zeolite framework on spectral features requires direct comparisons between experiment and DFT. As mentioned in the Introduction, computational vibrational spectroscopy can be a powerful tool for analyzing experiments, but one needs to be aware of the systematic errors that arise when using DFT. In light of this, we begin by mapping out all of the IR band locations for olefin I over a nonacidic zeolite (deAl-BEA in experiment; all-silica MOR in theory) to determine the nature of systematic error associated with our models. In particular, we created a parity plot (Figure 4a) using DFT-computed and experimental IR frequencies; Figure 4b highlights the signs and magnitudes of discrepancies in different regions of the IR spectrum. Figure 4 shows that in the lower-frequency region ( $1300\text{--}1700\text{ cm}^{-1}$ ), associated with C–C stretches and methyl deformations, DFT provides systematically red-shifted frequencies. In contrast, in the higher-frequency region ( $2800\text{--}3200\text{ cm}^{-1}$ ) associated with C–H stretches, the computed frequencies are blue-shifted from experiment. This pattern of systematic error, which has been observed by others,<sup>20,42</sup> allows us to make more informed comparisons between computed and experimental spectral features for interpretation of spectra and determining the impact of zeolite–guest interactions. Now, we consider experimental and computed spectra of molecule I in nonacidic zeolites.

We begin our interpretation of the IR spectra of olefin I by considering the DRIFTS over deAl-BEA. Figure 5 (bottom) shows the DRIFT spectrum (purple) of molecule I adsorbed over deAl-BEA at 20 °C, revealing several bands in both the low- and high-frequency regions of the spectrum. For the purpose of distinguishing between the two conformers, we focus on the C=C stretching region ( $1600\text{--}1700\text{ cm}^{-1}$ ) and the C–H stretching region ( $2800\text{--}3100\text{ cm}^{-1}$ ). Several overlapping bands are observed between  $1600\text{--}1700\text{ cm}^{-1}$  with observable maxima at 1601, 1629, and 1645  $\text{cm}^{-1}$  and a distinct shoulder at 1654  $\text{cm}^{-1}$ . The conjugated diene should exhibit two distinct bands in this region, associated with the symmetric and antisymmetric C=C stretches. Thus, the appearance of four bands suggests the existence of two stable conformers. In the C–H stretching region, we observe a single weak band at 3084  $\text{cm}^{-1}$  as well as a very weak intensity band at 3040  $\text{cm}^{-1}$ . Also, we note a strong band at 2971  $\text{cm}^{-1}$  with a weak shoulder at 3005  $\text{cm}^{-1}$ . Now we detail the corresponding computed IR spectra and compare them with those from the experiment to investigate the nature of zeolite–guest interactions and conformational populations of species I.

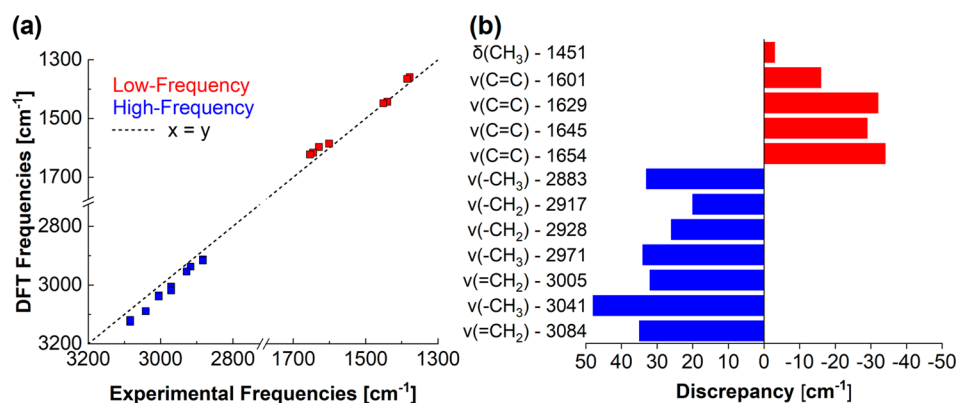


**Figure 4.** (a) Parity plot comparing experimental frequencies from DRIFTS of molecule I in deAl-BEA with DFT-computed frequencies of I over all-silica MOR. The parity line ( $x = y$ ) is shown to highlight the different discrepancies in high- (blue) and low-frequency (red) regions of the IR spectrum. (b) Bar graph showing signs and magnitudes of discrepancies between computed and experimental frequencies (the latter shown on the left of Figure 4b) along with their assignments.

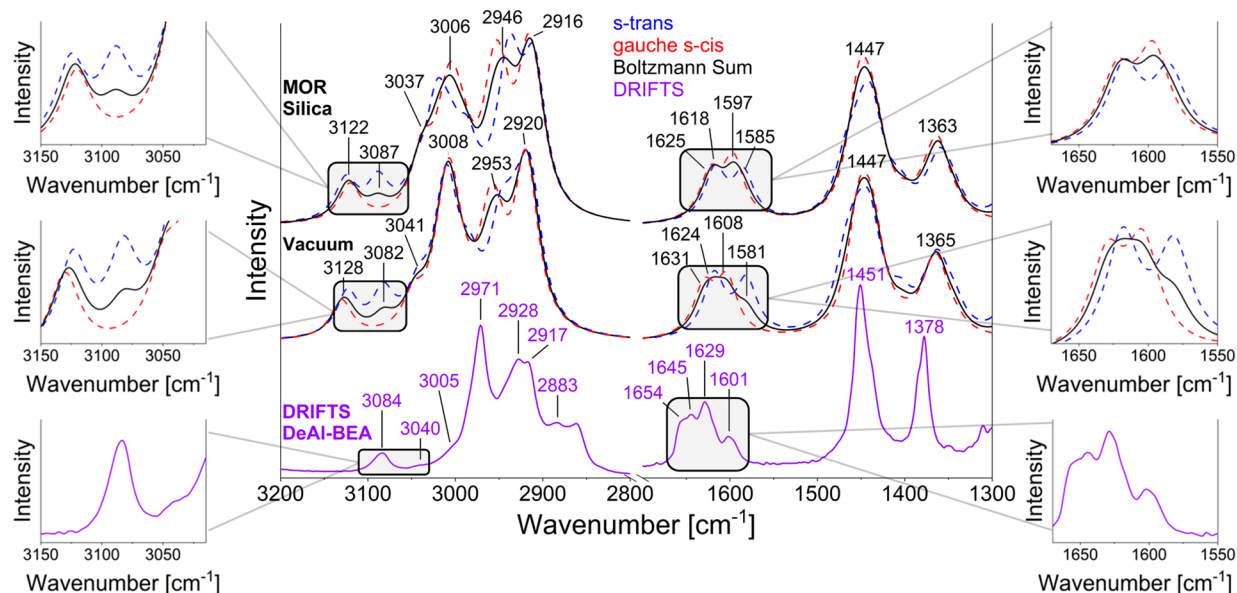


**Figure 5.** Comparison of computed and experimental spectra of molecule I. DRIFT spectrum (purple) was taken at 20 °C over deAl-BEA. Computed spectra for molecules I in all-silica MOR (top) and in gas phase (middle). In each environment, the spectrum associated with *s*-trans (blue), *gauche s*-cis (red), and the Boltzmann sum (black) are shown. Wavenumber values apply to Boltzmann sum. Side panels focus on (left) high-frequency (C–H stretch) and (right) low-frequency (C=C stretch) regions.

Turning to the computed spectra in Figure 5, the *gauche s*-cis and *s*-trans conformers exhibit distinct spectral features. Figure 5 shows computed IR spectra for *gauche s*-cis (red) and *s*-trans (blue) in vacuum (middle) and in all-silica MOR (top). We begin by discussing the C=C stretching bands in the lower-frequency region of the MOR spectrum (on the right of Figure 5). Within this region there are a total of four bands of which the 1597 and 1625  $\text{cm}^{-1}$  bands are associated with the *gauche s*-cis conformer, and the 1585 and 1618  $\text{cm}^{-1}$  bands are attributed to the *s*-trans conformer. The upper side panels on the right-hand side of Figure 5 highlight this region and show that the *gauche s*-cis bands are slightly blue-shifted from the *s*-trans bands. We also find that for the *gauche s*-cis conformer, the symmetric C=C stretch (1597  $\text{cm}^{-1}$ ) is at a lower frequency than the antisymmetric C=C stretch (1620  $\text{cm}^{-1}$ ). Interestingly, this pattern is opposite for the *s*-trans where the symmetric C=C stretch (1616  $\text{cm}^{-1}$ ) is higher in frequency than the antisymmetric band (1585  $\text{cm}^{-1}$ ). The combination

of these bands allows us to directly compare to the DRIFTS in the same region. We applied Boltzmann averaging of these conformer-specific spectra to produce an overall spectrum for comparison with experiment. In particular, based on the DFT-computed free energy difference stated above, the averaged spectrum in MOR has an *s*-trans:*s*-cis equilibrium ratio of 39:61 at 20 °C. Figure 5 shows the conformationally averaged spectra (black) for I in vacuum (middle) and all-silica MOR (top), both showing good qualitative agreement with DRIFTS of I in deAl-BEA. The positions of the DFT-computed C=C stretches are systematically red-shifted from the experimental vibrations (as shown in Figure 4), which allows us to assign the experimental bands to the respective conformers (see Table 1 for these assignments). For instance, the broad C=C stretching feature in the summed MOR spectrum exhibits some *s*-trans character giving rise to a small shoulder at 1585  $\text{cm}^{-1}$ , which we assign to the low-intensity band at 1601  $\text{cm}^{-1}$  in the DRIFTS. As such, within the C=C stretching region, there are

**Table 1.** Summary of Vibrational Band Assignments for Gauche *s*-cis and *s*-trans Conformers of Molecule I<sup>a</sup>

| Molecular Vibration                    | DRIFTS   |                 | Theory – CP2K   |                 |                 |  |
|--|----------|-----------------|-----------------|-----------------|-----------------|--|
|  | DeAl-BEA | MOR Silica      |                 | Vacuum          |                 |  |
|  |          | <i>g s</i> -cis | <i>s</i> -trans | <i>g s</i> -cis | <i>s</i> -trans |  |
| $\delta_{\text{sym}}(-\text{CH}_3)$    | 1378     | 1365            | 1359            | 1365            | 1363            |  |
| $\delta_{\text{asym}}(-\text{CH}_3)$   | 1451     | 1448            | 1443            | 1447            | 1445            |  |
| $\nu_{\text{asym}}(\text{C}=\text{C})$ | 1601     |                 | 1585            |                 | 1582            |  |
| $\nu_{\text{sym}}(\text{C}=\text{C})$  | 1629     | 1597            |                 | 1603            |                 |  |
| $\nu_{\text{sym}}(\text{C}=\text{C})$  | 1645     |                 | 1616            |                 | 1618            |  |
| $\nu_{\text{asym}}(\text{C}=\text{C})$ | 1654     | 1620            |                 | 1628            |                 |  |
| $\nu_{\text{sym}}(-\text{CH}_3)$       | 2883     | 2916            | 2913            | 2920            | 2918            |  |
| $\nu_{\text{asym}}(-\text{CH}_2)$      | 2917     |                 | 2937            |                 | 2944            |  |
| $\nu_{\text{asym}}(-\text{CH}_2)$      | 2928     | 2954            |                 | 2958            |                 |  |
| $\nu_{\text{asym}}(-\text{CH}_3)$      | 2971     | 3005            | 3018            | 3007            | 3010            |  |
| $\nu_{\text{sym}}(=\text{CH}_2)$       | 3005     | 3035            | 3039            | 3042            | 3038            |  |
| $\nu_{\text{asym}}(-\text{CH}_3)$      | 3040     |                 | 3087            |                 | 3082            |  |
| $\nu_{\text{asym}}(-\text{CH}_2)$      | 3084     | 3119            | 3125            | 3131            | 3124            |  |

<sup>a</sup>Frequency values from the DRIFT spectrum over deAl-BEA are shown. Each band is associated with either the gauche *s*-cis or *s*-trans conformer as determined by comparison with computed frequencies, as highlighted by the light blue boxes.

a total of four bands associated with two distinct conformers of olefin I, which we have distinguished by comparison of the DRIFTS with the Boltzmann-averaged computed spectrum. Our analysis shows that the overall shape of the DRIFTS in the low-frequency regions clearly indicates the presence of both *s*-trans and gauche *s*-cis conformers in appreciable populations, with slight preference for the gauche *s*-cis conformer.

The distinguishing of the two conformers of I is further carried out by considering the bands in the C–H stretching region. The left-side panels of Figure 5 focus on this region of the spectrum, around 3100 cm<sup>-1</sup>. The DFT-computed MOR spectrum (Figure 5; top) of the *s*-trans conformer (blue) exhibits two bands at 3125 and 3087 cm<sup>-1</sup> of nearly equal intensity, while the spectrum of the gauche *s*-cis conformer (red) has only a single band at 3119 cm<sup>-1</sup>. The overlapping bands at around 3122 cm<sup>-1</sup> are associated with an antisymmetric =CH<sub>2</sub> stretch, which is present in both conformers. In contrast, the band at 3087 cm<sup>-1</sup> is only present in the *s*-trans conformer, and through visualization of its normal mode, we find it is associated with an asymmetric CH<sub>3</sub> stretch. While a frequency value of 3087 cm<sup>-1</sup> for an asymmetric CH<sub>3</sub> is on the high end of the expected range, such high frequencies have been reported in previous studies that also considered this region of the spectrum.<sup>43,44</sup> Both conformers also exhibit strong bands near 3006 cm<sup>-1</sup> with a shoulder at 3037 cm<sup>-1</sup> attributed to an asymmetric CH<sub>3</sub> stretch and a symmetric =CH<sub>2</sub> stretch, respectively. Analyzing the Boltzmann-summed MOR spectrum of the two conformers (Figure 5 top; black), we find that incorporating the *s*-trans species gives rise to a low intensity band at 3087 cm<sup>-1</sup> in addition to a higher intensity band at 3122 cm<sup>-1</sup>, the latter being associated with both conformers. The mapping of these features to experiment is facilitated by recalling that the positions of the DFT-computed C–H stretches are systematically blue-shifted from the experimental vibrations (as shown in Figure 4). The 3087 cm<sup>-1</sup> computed band of the *s*-trans species is attributed to the low-intensity experimental feature at 3040 cm<sup>-1</sup>, while the 3122 cm<sup>-1</sup> computed band maps on to the 3084 cm<sup>-1</sup> DRIFTS band. The relative intensities of the computed bands at 3122 and 3087 cm<sup>-1</sup> in the Boltzmann sum spectrum closely resemble those of the experimentally observed bands at 3084 and 3040 cm<sup>-1</sup>, respectively. Despite

the discrepancies between theory and experiment, the systematic pattern of error enables unambiguous assignments of peaks in the DRIFTS to the gauche *s*-cis and *s*-trans conformers of olefin I by comparison with computed spectra.

Overall, we demonstrate that our DFT-computed models allow for the interpretation of experimental IR spectra of conformers of olefin I in deAl-BEA. Complete assignments of observed experimental and DFT-computed bands are summarized in Table 1. By computing IR spectra of gauche *s*-cis and *s*-trans conformers along with their relative free energies, we have constructed a useful representation of the experimental DRIFT spectrum, corroborating the presence of both conformers and the surprising abundance of the gauche *s*-cis conformer. Additionally, the comparison of vacuum and zeolite-adsorbed computed band positions in Table 1 reveals very small differences, on the order of ±5 cm<sup>-1</sup>, thus suggesting very weak zeolite–guest interactions for I in all-silica MOR as seen through the lens of IR spectroscopy (see Supporting Information Section SI 5 for further discussion on this point). We now turn to the study of olefins I and II in the acidic zeolite HMOR to determine the strength of zeolite–guest interactions in that system.

**3.2. Adsorption of Neutral Acyclic Olefins on Acidic HMOR Zeolite: Strong Interactions Lead to Protonation.** We next studied the adsorption of polyenes I and II on the acidic zeolite HMOR via IR spectroscopy. Previous studies have found that certain olefins have high proton affinities, suggesting that their protonation in acidic zeolites is thermodynamically favored.<sup>45</sup> As a result, we may expect strong interactions between olefins I/II and the HMOR Brønsted acid site. The question remains how such strong interactions manifest in the IR spectra of these zeolite–guest systems. Figure 6 shows DRIFT spectra (in black) in the 1300–1700 cm<sup>-1</sup> region for species I (Figure 6a) and II (Figure 6b) in HMOR at 20 °C. There are two main spectral features for both zeolite–guest systems: (1) a strong singlet in the 1500–1600 cm<sup>-1</sup> region and (2) a broad doublet in the 1300–1400 cm<sup>-1</sup> region. Bands at 1372 cm<sup>-1</sup> (I) and 1383 cm<sup>-1</sup> (II) are assigned to methyl deformations.<sup>46</sup> The strong singlets observed at 1548 cm<sup>-1</sup> (I) and 1568 cm<sup>-1</sup> (II) are characteristic of allylic cations  $\nu(\text{C}=\text{C}-\text{C}^+)$ ,<sup>47,48</sup> suggesting that protonation has taken place for both guests in HMOR.

To determine the atomic-level nature of the adsorbed states of olefins I and II in HMOR, we show in Figures 6a and 6b, respectively, the computed IR spectra from periodic DFT using the full optimization method. For each zeolite–guest system, we show IR spectra computed from a neutral olefin hydrogen-bonded to the Brønsted acid site (in orange) and from a protonated olefin (I<sup>+</sup>/II<sup>+</sup>) interacting electrostatically with the zeolite conjugate base (in blue). The protonated forms I<sup>+</sup> and II<sup>+</sup> were obtained by manually protonating the neutral counterparts at the lowest energy protonation site determined by gas-phase electronic structure calculations (see Figure S6 and Table S2 in Supporting Information). The calculated Gibbs energies of the various protonated forms indicate that protonation is preferred at the carbon that produces a conjugated allylic cation system that is fully alkyl substituted at the terminal carbons. As in the section Section 3.1, we considered the various conformations for molecule II<sup>+</sup>. (Note that molecule I<sup>+</sup> exhibits only a single conformation because of the symmetry conferred by protonation.) For molecule II<sup>+</sup>, however, we considered a total of eight possible conformers (see Table S3) and found that the all-trans conformer is

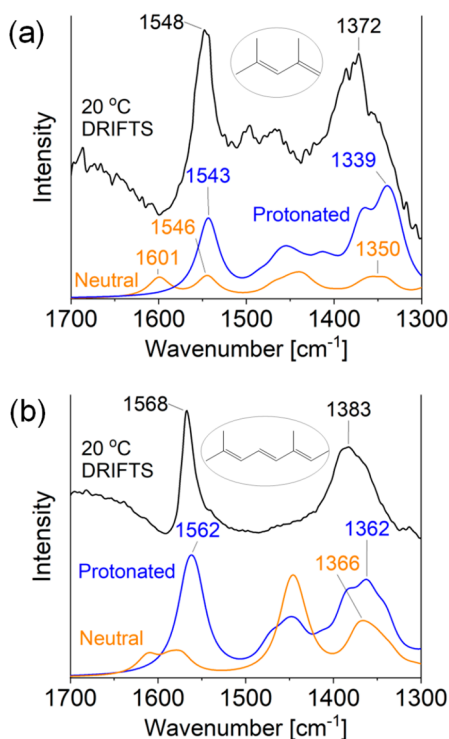


**Figure 6.** DRIFT spectra at 20 °C (black) for guest molecules (a) I and (b) II in HMOR zeolite. Shown for comparison are zeolite-adsorbed, computed spectra using full optimization of neutral (orange) and protonated (blue) forms of each molecule.

strongly energetically favored. Thus, in this case, considering the spectrum for only the all-trans conformer is sufficient. Qualitatively comparing the experimental and computed spectra in Figure 6a strongly suggests that olefin I is protonated in HMOR; the same conclusion can be drawn for olefin II from the data in Figure 6b. In particular, both computed IR spectra for the protonated olefins in Figure 6 show the strong band in the 1500–1600  $\text{cm}^{-1}$  region and the broader band in the 1300–1400  $\text{cm}^{-1}$  region. In contrast, the computed IR spectra for the neutral olefins in HMOR retain the bands around 1600  $\text{cm}^{-1}$ , corresponding to C=C stretching vibrations, which were also seen in the spectra in Section 3.1 (Figure 5). Also, in contrast to the IR spectrum of I in all-silica MOR, the bands in HMOR are red-shifted (and double bonds lengthened by about 0.05 Å compared to gas-phase values) because of hydrogen bonding with the Brønsted acid site.

Quantitative comparisons between theory and experiment in Figure 6 also support the notion of protonated olefins in HMOR. The strong singlet bands from computed spectra in Figure 6 are seen at 1543  $\text{cm}^{-1}$  (I<sup>+</sup>) and 1562  $\text{cm}^{-1}$  (II<sup>+</sup>), respectively, which compare well with experimental values of 1548 and 1568  $\text{cm}^{-1}$ , indicating that our fully optimized periodic DFT approach has captured the blue shift in the IR spectrum from I<sup>+</sup> to II<sup>+</sup>. Visual inspection<sup>49</sup> of normal modes for these vibrations do indeed indicate motions of allylic cations (C=C–C<sup>+</sup>),<sup>47,48</sup> as shown in Figure 7 for species I<sup>+</sup>. We were curious whether the small, systematic error of 5–6  $\text{cm}^{-1}$  could be attributed to finite temperature effects. To address this, we employed the ensemble averaging model and found that thermal fluctuations of the zeolite at experimental temperatures of 20, 130, and 200 °C do not significantly impact the spectrum in the key spectral region of 1300–1700

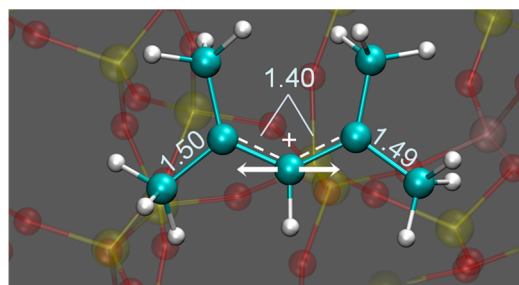


**Figure 7.** Illustration of I<sup>+</sup> adsorbed over HMOR zeolite. Fully optimized geometry is shown with equilibrium bond distances [Å]. White arrow designates the vibrational motion associated with the 1543  $\text{cm}^{-1}$  peak in the computed spectrum.

$\text{cm}^{-1}$  (see Figure S7 in Supporting Information). Furthermore, we found that the spread of spectra in the ensembles at 20 and 200 °C was nearly identical (Figure S8 in Supporting Information). Finally, we note that our computed bands for methyl deformations at 1339 and 1362  $\text{cm}^{-1}$  for molecule I<sup>+</sup> and II<sup>+</sup>, respectively, show very good qualitative agreement in band shapes with experimental DRIFTS data, though the computed band locations are red-shifted compared to experiment. Thus, the spectra in Figure 6 suggest that fully optimized periodic DFT within the harmonic approximation captures the key features of the IR spectra at 20 °C and that both olefins in HMOR exhibit spectral bands consistent with protonated states.

As a final test of this idea, we evaluated the Helmholtz free energies of protonation for I and II in HMOR within the multidimensional harmonic oscillator model using the formula shown in Figure S4 of Supporting Information. We found Helmholtz free energies of protonation of –18.0 and –27.3 kcal/mol for I and II, respectively, further supporting the IR spectroscopy findings of protonation in HMOR at 20 °C. The definitive computational test would be to find relatively low protonation barriers, allowing facile protonation at 20 °C. We leave this for future work. We nonetheless conclude from the thermodynamics and spectroscopy findings described herein that olefins I and II become protonated in HMOR at 20 °C, representing an example of strong zeolite–guest interaction.

**3.3. Adsorbed Protonated Olefins on HMOR: Nature of Electrostatic Interactions.** We found above that the adsorption of acyclic olefins I and II on HMOR results in significant changes to the IR spectra in the 1300–1700  $\text{cm}^{-1}$  region, attributed to protonation from Brønsted acid sites in HMOR. Such protonation leaves behind an ion-pair interaction between the protonated olefin and the conjugate base of the acidic zeolite. It is interesting to determine how this ion-pair electrostatic interaction may influence the IR spectra of the zeolite–guest systems.

Figure 8 addresses this question by comparing the computed spectra of protonated molecules I<sup>+</sup> (Figure 8a) and II<sup>+</sup> (Figure 8b) in the gas phase (red) and in MOR<sup>–</sup> (blue). We applied the same level of theory (BLYP) and basis set (triple- $\zeta$  valence polarized) in gas-phase and zeolite-adsorbed calculations to produce appropriate comparisons. We found the remarkable and perhaps surprising result for cation I<sup>+</sup> in Figure 8a that the zeolite-adsorbed cation and gas-phase cation exhibit essentially the same IR spectra in the key 1300–1700  $\text{cm}^{-1}$  region, with only tiny shifts within the margin of error of the DFT method and largely minor variations in the intensity distribution. Figure 8b shows the same surprising result for cation II<sup>+</sup>. In the

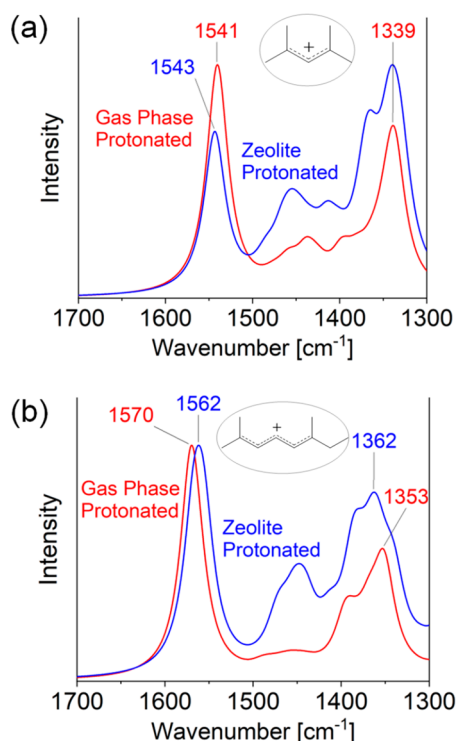


**Figure 8.** Comparison of computed gas-phase (red) and zeolite-adsorbed (blue) spectra for molecules (a)  $I^+$  and (b)  $II^+$ .

case of  $I^+$ , a singlet is seen at  $1541\text{ cm}^{-1}$  in the gas-phase spectrum, which is within a few wavenumbers from the zeolite-adsorbed band. Similarly, the gas-phase singlet for  $II^+$  at  $1570\text{ cm}^{-1}$  is only  $8\text{ cm}^{-1}$  from the zeolite-adsorbed band. Furthermore, inspection of the relevant normal modes for  $I^+$  and  $II^+$  revealed that the vibration corresponding to these singlets is identical in the gas phase and the zeolite, namely, the allylic stretching mentioned in the previous section (see Figure 7). A structural analysis demonstrates that the intramolecular configurations of  $I^+$  and  $II^+$  are essentially unchanged upon adsorption, as highlighted in Figure S9 in the Supporting Information for molecule  $II^+$ . Thus, despite the presence of an electrostatic ion-pair interaction between the protonated olefins and the negatively charged zeolite conjugate base, the structures and IR spectra of these olefins appear unaffected by the zeolite. In other words, our results suggest the finding that in order to model the spectral fingerprints in the  $1300\text{--}1700\text{ cm}^{-1}$  region of acyclic olefins over acidic zeolites with a margin of error of  $10\text{ cm}^{-1}$ , one only needs to consider the protonated species in the gas phase.

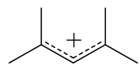
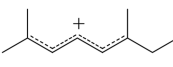
Table 2 presents a summary of the aforementioned computed frequencies of protonated olefins  $I^+$  and  $II^+$  alongside experimental values for comparison. We note two important findings from these comparisons. The first finding pertains to the systematic red-shifting of computational bands relative to experimental ones, consistent with results in Figure 4 and Table 1. A combination of data in Tables 1 and 2 reveals the second and more remarkable finding that including the zeolite framework when computing the IR spectrum may not significantly increase the agreement between theory and experiment. We examined this by computing absolute differences between experiment and each of the models in both Tables 1 and 2 and then constructing root-mean-square (RMS) differences considering all vibrations in the Tables. This yields RMS differences of 25.8, 27.4, and  $31.1\text{ cm}^{-1}$  for CP2K Vacuum, CP2K MOR adsorbed, and Gaussian gas phase, respectively. We conclude then that for these acyclic olefins adsorbed on acidic and nonacidic zeolites, modeling the regions of the IR spectrum studied in our work can be accomplished by simply treating the molecule in the gas phase.

#### 4. CONCLUSIONS

We performed experimental IR measurements and periodic DFT calculations on acyclic olefins in acidic HMOR zeolite and nonacidic porous silica to investigate the nature of adsorbed species and the influence of host–guest interaction on the IR spectra. In particular, we studied the acyclic olefins 2,4-dimethyl-1,3-pentadiene ( $I$ ) and 2,6-dimethyl-2,4,6-octatriene ( $II$ ) because of their importance in the field of methanol conversion, as precursors to cyclic intermediates that (i) are active in the catalytic cycle and (ii) can lead to deactivating species known as “coke.” We found that a  $1 \times 1 \times 2$  supercell of HMOR was necessary to avoid spurious interactions between guests in neighboring periodic images. A BLYP functional with a triple- $\zeta$  valence polarized basis set was used within the CP2K software. For the computation of zeolite-adsorbed IR spectra, we employed two techniques within the harmonic approximation: (1) full optimization followed by normal-mode analysis (NMA) and (2) an ensemble averaging scheme that takes into account thermal fluctuations of the zeolite. We used these models to compare with diffuse reflectance Fourier transform (DRIFT) spectra to investigate the impact on IR spectra of host–guest interactions and the state of the adsorbed acyclic olefin.

We employed DFT-based thermodynamics calculations and found the surprising result that for olefin  $I$  adsorbed over all-silica, large-pore zeolites, a gauche *s-cis* conformer is slightly preferred over its *s-trans* counterpart. We found that this slight

**Table 2.** Summary of Computed Frequencies ( $\text{cm}^{-1}$ ) for Protonated Olefins  $I^+$  and  $II^+$  in the Gas Phase and Inside HMOR Zeolite<sup>a</sup>

| Molecule  | Molecular Vibration                | DRIFTS | CP2K | Gaussian |
|---|------------------------------------|--------|------|----------|
|   |                                    |        | HMOR | Gas      |
|  | $\nu(\text{C}=\text{C}^+)$         | 1548   | 1543 | 1541     |
|   | $\delta_{\text{sym}}(\text{CH}_3)$ | 1372   | 1339 | 1339     |
|  | $\nu(\text{C}=\text{C}^+)$         | 1568   | 1562 | 1570     |
|   | $\delta_{\text{sym}}(\text{CH}_3)$ | 1383   | 1362 | 1353     |

<sup>a</sup>Experimental DRIFTS frequencies are shown for comparison for the olefins adsorbed on HMOR.

preference toward the gauche *s*-cis conformer was reflected in the experimental IR spectrum, which was accurately represented by using a Boltzmann-weighted sum of the computed spectra of each conformer. Next, we found that the introduction of olefins I and II into the acidic zeolite HMOR produced substantial changes to the IR spectra, showing the signature of protonated species such as a strong singlet in the 1500–1600  $\text{cm}^{-1}$  region typically assigned to stretching of allylic cations,  $\nu(\text{C}=\text{C}-\text{C}^+)$ . Periodic DFT using the full optimization model on protonated guests ( $\text{I}^+$  and  $\text{II}^+$ ) was found to accurately represent the DRIFT spectra in HMOR at 20 °C. The computed IR spectra were essentially unchanged from including zeolite atoms in the NMA, and from including thermal fluctuations of the zeolite, suggesting that system optimization and guest NMA are sufficient to capture IR spectra of acyclic olefins in acidic zeolites. Thermodynamics calculations based on the periodic DFT results are consistent with the stability of the protonated state of olefins I and II in zeolite HMOR.

To determine the influence of electrostatic interactions between cationic guests ( $\text{I}^+$  and  $\text{II}^+$ ) and negatively charged zeolites, we compared IR spectra computed for zeolite-adsorbed and gas-phase cations, finding virtually no difference in the spectra in the 1300–1700  $\text{cm}^{-1}$  region. Structural analyses of bond lengths and dihedral angles of zeolite-adsorbed and gas-phase alkenyl and alkadienyl cations support the notion that ion-pair electrostatic interactions have negligible effect on these cations in zeolites. An analysis of the discrepancies between experimental IR frequencies for various vibrational modes and those from our models suggests the surprising finding that gas-phase models of zeolite adsorption are both the most efficient and in certain instances, such as for allylic stretching modes, just as accurate as zeolite-adsorbed models as long as the relevant state of the guest is taken into account.

## ■ ASSOCIATED CONTENT

### Supporting Information

The Supporting Information is available free of charge at <https://pubs.acs.org/doi/10.1021/acs.jpcc.0c01225>.

Characterization of zeolites used in the experiments; results from inclusion of zeolite framework in NMA analysis; thermodynamics of periodic DFT systems; free energy profiles for rotational conformers of olefin I; liquid film data for olefin I; thermodynamics of protonation for olefins I and II; conformational analysis for olefin  $\text{II}^+$ ; impact of thermal fluctuations on vibrational spectra; intramolecular bond distances and dihedrals for protonated olefin in the gas phase and zeolite; atomic coordinates for key structures studied in gas-phase and periodic DFT calculations (PDF)

## ■ AUTHOR INFORMATION

### Corresponding Authors

**Scott M. Auerbach** – Department of Chemistry and Department of Chemical Engineering, University of Massachusetts Amherst, Amherst, Massachusetts 01003, United States; [orcid.org/0000-0001-8598-3082](https://orcid.org/0000-0001-8598-3082); Email: [auerbach@umass.edu](mailto:auerbach@umass.edu)

**Friederike C. Jentoft** – Department of Chemical Engineering, University of Massachusetts Amherst, Amherst, Massachusetts

01003, United States; [orcid.org/0000-0003-4123-0454](https://orcid.org/0000-0003-4123-0454); Email: [fcjentoft@umass.edu](mailto:fcjentoft@umass.edu)

### Authors

**Babgen Manookian** – Department of Chemistry, University of Massachusetts Amherst, Amherst, Massachusetts 01003, United States; [orcid.org/0000-0002-6273-0995](https://orcid.org/0000-0002-6273-0995)

**Eric D. Hernandez** – Department of Chemical Engineering, University of Massachusetts Amherst, Amherst, Massachusetts 01003, United States; [orcid.org/0000-0001-6549-1179](https://orcid.org/0000-0001-6549-1179)

**Marcel D. Baer** – Physical and Computational Sciences Directorate, Pacific Northwest National Laboratory, Richland, Washington 99352, United States

**Christopher J. Mundy** – Physical and Computational Sciences Directorate, Pacific Northwest National Laboratory, Richland, Washington 99352, United States; Department of Chemical Engineering, University of Washington, Seattle, Washington 98195, United States; [orcid.org/0000-0003-1378-5241](https://orcid.org/0000-0003-1378-5241)

Complete contact information is available at: <https://pubs.acs.org/doi/10.1021/acs.jpcc.0c01225>

### Notes

The authors declare no competing financial interest.

## ■ ACKNOWLEDGMENTS

B.M. and S.M.A. were supported by the National Science Foundation under Award # CBET-1512442. Acknowledgment is made to the Donors of the American Chemical Society Petroleum Research Fund for support (or partial support) of this research (#589978-NDS, E.D.H. and F.C.J.). M.D.B. was supported by the US Department of Energy (DOE), Office of Science, Office of Basic Energy Sciences (BES), Division of Materials Science and Engineering. C.J.M. was supported by the DOE, Office of Science, BES, Division of Chemical Sciences, Geosciences, and Biosciences. Pacific Northwest National Laboratory (PNNL) is a multiprogram national laboratory operated by Battelle for the U.S. DOE. Computing resources were generously provided through PNNL's institutional computing (PIC).

## ■ REFERENCES

- (1) Yarulina, I.; Chowdhury, A. D.; Meirer, F.; Weckhuysen, B. M.; Gascon, J. Recent Trends and Fundamental Insights in the Methanol-to-Hydrocarbons Process. *Nat. Catal.* **2018**, *1* (6), 398–411.
- (2) Lehman, S. E.; Larsen, S. C. Zeolite and Mesoporous Silica Nanomaterials: Greener Syntheses, Environmental Applications and Biological Toxicity. *Environ. Sci.: Nano* **2014**, *1* (3), 200–213.
- (3) Migues, A. N.; Sun, Q.; Vaitheeswaran, S.; Sherman, W.; Auerbach, S. M. On the Rational Design of Zeolite Clusters for Converging Reaction Barriers: Quantum Study of Aldol Kinetics Confined in HZSM-5. *J. Phys. Chem. C* **2018**, *122* (40), 23230–23241.
- (4) Liu, B.; Slocombe, D.; AlKinany, M.; AlMegren, H.; Wang, J.; Arden, J.; Vai, A.; Gonzalez-Cortes, S.; Xiao, T.; Kuznetsov, V.; et al. Advances in the Study of Coke Formation over Zeolite Catalysts in the Methanol-to-Hydrocarbon Process. *Appl. Petrochem. Res.* **2016**, *6*, 1–7.
- (5) Olsbye, U.; Svelle, S.; Lillerud, K. P.; Wei, Z. H.; Chen, Y. Y.; Li, J. F.; Wang, J. G.; Fan, W. B. The Formation and Degradation of Active Species during Methanol Conversion over Protonated Zeotype Catalysts. *Chem. Soc. Rev.* **2015**, *44* (20), 7155–7176.
- (6) Daniel, D.; Konstantin, R.; Wladimir, R. Experimental and Computational Investigations of the Deactivation of H-ZSM-5 Zeolite by Coking in the Conversion of Ethanol into Hydrocarbons. *ChemCatChem* **2012**, *4* (6), 802–814.

- (7) Bjørgen, M.; Akyalcin, S.; Olsbye, U.; Benard, S.; Kolboe, S.; Svelle, S. Methanol to Hydrocarbons over Large Cavity Zeolites: Toward a Unified Description of Catalyst Deactivation and the Reaction Mechanism. *J. Catal.* **2010**, *275* (1), 170–180.
- (8) Goetze, J.; Weckhuysen, B. M. Spatiotemporal Coke Formation over Zeolite ZSM-5 during the Methanol-to-Olefins Process as Studied with Operando UV-Vis Spectroscopy: A Comparison between H-ZSM-5 and Mg-ZSM-5. *Catal. Sci. Technol.* **2018**, *8* (6), 1632–1644.
- (9) Park, J. W.; Seo, G. IR Study on Methanol-to-Olefin Reaction over Zeolites with Different Pore Structures and Acidities. *Appl. Catal., A* **2009**, *356* (2), 180–188.
- (10) Stavitski, E.; Pidko, E. A.; Kox, M. H. F.; Hensen, E. J. M.; van Santen, R. A.; Weckhuysen, B. M. Detection of Carbocationic Species in Zeolites: Large Crystals Pave the Way. *Chem. - Eur. J.* **2010**, *16* (31), 9340–9348.
- (11) Osuga, R.; Yokoi, T.; Kondo, J. N. IR Observation of Activated Ether Species on Acidic OH Groups on H-ZSM-5 Zeolites. *Mol. Catal.* **2019**, *477*, 110535.
- (12) Hemelsoet, K.; Van der Mynsbrugge, J.; De Wispelaere, K.; Waroquier, M.; Van Speybroeck, V. Unraveling the Reaction Mechanisms Governing Methanol-to-Olefins Catalysis by Theory and Experiment. *ChemPhysChem* **2013**, *14* (8), 1526–1545.
- (13) De Moor, B. A.; Ghysels, A.; Reyniers, M.-F.; Van Speybroeck, V.; Waroquier, M.; Marin, G. B. Normal Mode Analysis in Zeolites: Toward an Efficient Calculation of Adsorption Entropies. *J. Chem. Theory Comput.* **2011**, *7* (4), 1090–1101.
- (14) Dahl, I. M.; Kolboe, S. On the Reaction Mechanism for Propene Formation in the MTO Reaction over SAPO-34. *Catal. Lett.* **1993**, *20* (3), 329–336.
- (15) Wulfers, M. J.; Jentoft, F. C. The Role of Cyclopentadienium Ions in Methanol-to-Hydrocarbons Chemistry. *ACS Catal.* **2014**, *4* (10), 3521–3532.
- (16) Borodina, E.; Sharbini Harun Kamaluddin, H.; Meirer, F.; Mokhtar, M.; Asiri, A. M.; Al-Thabaiti, S. A.; Basahel, S. N.; Ruiz-Martinez, J.; Weckhuysen, B. M. Influence of the Reaction Temperature on the Nature of the Active and Deactivating Species During Methanol-to-Olefins Conversion over H-SAPO-34. *ACS Catal.* **2017**, *7* (8), 5268–5281.
- (17) Joshi, Y. V.; Thomson, K. T. Embedded Cluster (QM/MM) Investigation of C<sub>6</sub> Diene Cyclization in HZSM-5. *J. Catal.* **2005**, *230* (2), 440–463.
- (18) Marchese, L.; Frache, A.; Gianotti, E.; Martra, G.; Causà, M.; Coluccia, S. ALPO-34 and SAPO-34 Synthesized by Using Morpholine as Templating Agent. FTIR and FT-Raman Studies of the Host-Guest and Guest-Guest Interactions within the Zeolitic Framework. *Microporous Mesoporous Mater.* **1999**, *30* (1), 145–153.
- (19) Sacchetto, V.; Olivás Olivera, D. F.; Paul, G.; Gatti, G.; Braschi, I.; Marchese, L.; Bisio, C. On the Adsorption of Gaseous Mixtures of Hydrocarbons on High Silica Zeolites. *J. Phys. Chem. C* **2017**, *121* (11), 6081–6089.
- (20) Mathias, G.; Baer, M. D. Generalized Normal Coordinates for the Vibrational Analysis of Molecular Dynamics Simulations. *J. Chem. Theory Comput.* **2011**, *7* (7), 2028–2039.
- (21) Hemelsoet, K.; Ghysels, A.; Mores, D.; De Wispelaere, K.; Van Speybroeck, V.; Weckhuysen, B. M.; Waroquier, M. Experimental and Theoretical IR Study of Methanol and Ethanol Conversion over H-SAPO-34. *Catal. Today* **2011**, *177* (1), 12–24.
- (22) Agarwal, V.; Huber, G. W.; Conner, W. C.; Auerbach, S. M. Simulating Infrared Spectra and Hydrogen Bonding in Cellulose I $\beta$  at Elevated Temperatures. *J. Chem. Phys.* **2011**, *135* (13), 134506.
- (23) Burbidge, B. W.; Keen, I. M.; Eyles, M. K. Physical and Catalytic Properties of the Zeolite Mordenite. In *Molecular Sieve Zeolites-II*; Advances in Chemistry; American Chemical Society, 1971; Vol. 102, pp 71–400. doi: DOI: 10.1021/ba-1971-0102.ch071.
- (24) O'Donovan, A. W.; O'Connor, C. T.; Koch, K. R. Effect of Acid and Steam Treatment of Na- and H-Mordenite on Their Structural, Acidic and Catalytic Properties. *Microporous Mater.* **1995**, *5* (4), 185–202.
- (25) Müller, M.; Harvey, G.; Prins, R. Comparison of the Dealumination of Zeolites Beta, Mordenite, ZSM-5 and Ferrierite by Thermal Treatment, Leaching with Oxalic Acid and Treatment with SiCl<sub>4</sub> by <sup>1</sup>H, <sup>29</sup>Si and <sup>27</sup>Al MAS NMR. *Microporous Mesoporous Mater.* **2000**, *34* (2), 135–147.
- (26) Baerlocher, C.; McCusker, L. B.; Olson, D. H. *Atlas of Zeolite Framework Types*, Sixth Edit.; Elsevier Science B.V.: Amsterdam, 2007.
- (27) Meier, W. M. The Crystal Structure of Mordenite (Ptilolite)\*. *Zeitschrift für Krist.* **1961**, *115* (5–6), 439–450.
- (28) Demuth, T.; Hafner, J.; Benco, L.; Toulhoat, H. Structural and Acidic Properties of Mordenite. An Ab Initio Density-Functional Study. *J. Phys. Chem. B* **2000**, *104* (19), 4593–4607.
- (29) Guo, H.; Ren, J.; Feng, G.; Li, C.; Peng, X.; Cao, D. Distribution of Al and Adsorption of NH<sub>3</sub> in Mordenite: A Computational Study. *J. Fuel Chem. Technol.* **2014**, *42* (5), 582–590.
- (30) Rasmussen, D. B.; Christensen, J. M.; Temel, B.; Studt, F.; Moses, P. G.; Rossmeisl, J.; Riisager, A.; Jensen, A. D. Reaction Mechanism of Dimethyl Ether Carbonylation to Methyl Acetate over Mordenite – a Combined DFT/Experimental Study. *Catal. Sci. Technol.* **2017**, *7* (5), 1141–1152.
- (31) Alberti, A.; Davoli, P.; Vezzolini, G. The Crystal Structure Refinement of a Natural Mordenite. *Z. Kristallogr. - Cryst. Mater.* **1986**, *175*, 249–256.
- (32) VandeVondele, J.; Krack, M.; Mohamed, F.; Parrinello, M.; Chassaing, T.; Hutter, J. QUICKSTEP: Fast and Accurate Density Functional Calculations Using a Mixed Gaussian and Plane Waves Approach. *Comput. Phys. Commun.* **2005**, *167* (2), 103–128.
- (33) Buczek, A.; Kupka, T.; Broda, M. A.; Żyła, A. Predicting the Structure and Vibrational Frequencies of Ethylene Using Harmonic and Anharmonic Approaches at the Kohn-Sham Complete Basis Set Limit. *J. Mol. Model.* **2016**, *22* (1), 42.
- (34) Grimme, S.; Antony, J.; Ehrlich, S.; Krieg, H. A Consistent and Accurate Ab Initio Parametrization of Density Functional Dispersion Correction (DFT-D) for the 94 Elements H-Pu. *J. Chem. Phys.* **2010**, *132* (15), 154104.
- (35) Goedecker, S.; Teter, M.; Hutter, J. Separable Dual-Space Gaussian Pseudopotentials. *Phys. Rev. B: Condens. Matter Mater. Phys.* **1996**, *54* (3), 1703–1710.
- (36) VandeVondele, J.; Hutter, J. Gaussian Basis Sets for Accurate Calculations on Molecular Systems in Gas and Condensed Phases. *J. Chem. Phys.* **2007**, *127* (11), 114105.
- (37) Frisch, M. J.; Trucks, G. W.; Schlegel, H. B.; Scuseria, G. E.; Robb, M. A.; Cheeseman, J. R.; Scalmani, G.; Barone, V.; Mennucci, B.; Petersson, G. A.; et al. *Gaussian 09*, Revision B.01; Gaussian Inc.: Wallingford, CT, 2009.
- (38) *NIST Computational Chemistry Comparison and Benchmark Database*, Release 20.; Johnson, III, R. D., Ed.; 2019.
- (39) Wang, T.; Luo, S.; Tompsett, G. A.; Timko, M. T.; Fan, W.; Auerbach, S. M. Critical Role of Tricyclic Bridges Including Neighboring Rings for Understanding Raman Spectra of Zeolites. *J. Am. Chem. Soc.* **2019**, *141* (51), 20318–20324.
- (40) Squillacote, M. E.; Liang, F. Conformational Thermodynamic and Kinetic Parameters of Methyl-Substituted 1,3-Butadienes. *J. Org. Chem.* **2005**, *70* (17), 6564–6573.
- (41) Sun, Y.; Zhou, C.-W.; Somers, K. P.; Curran, H. J. Ab Initio/Transition-State Theory Study of the Reactions of C<sub>5</sub>H<sub>9</sub> Species of Relevance to 1,3-Pentadiene, Part I: Potential Energy Surfaces, Thermochemistry, and High-Pressure Limiting Rate Constants. *J. Phys. Chem. A* **2019**, *123* (42), 9019–9052.
- (42) Rauhut, G.; Pulay, P. Transferable Scaling Factors for Density Functional Derived Vibrational Force Fields. *J. Phys. Chem.* **1995**, *99* (10), 3093–3100.
- (43) Tyrode, E.; Rutland, M. W.; Bain, C. D. Adsorption of CTAB on Hydrophilic Silica Studied by Linear and Nonlinear Optical Spectroscopy. *J. Am. Chem. Soc.* **2008**, *130* (51), 17434–17445.
- (44) Premadasa, U. I.; Moradighadi, N.; Kotturi, K.; Nonkumwong, J.; Khan, M. R.; Singer, M.; Masson, E.; Cimatu, K. L. A. Solvent

Isotopic Effects on a Surfactant Headgroup at the Air–Liquid Interface. *J. Phys. Chem. C* **2018**, *122* (28), 16079–16085.

(45) Fang, H.; Zheng, A.; Xu, J.; Li, S.; Chu, Y.; Chen, L.; Deng, F. Theoretical Investigation of the Effects of the Zeolite Framework on the Stability of Carbenium Ions. *J. Phys. Chem. C* **2011**, *115* (15), 7429–7439.

(46) Lin-Vien, D.; Colthup, N. B.; Fateley, W. G.; Grasselli, J. G. *The Handbook of Infrared and Raman Characteristic Frequencies of Organic Molecules*; Academic Press: San Diego, 1991; pp 9–28. DOI: [10.1016/B978-0-08-057116-4.50008-0](https://doi.org/10.1016/B978-0-08-057116-4.50008-0).

(47) Adam, W.; Casades, I.; Fornés, V.; García, H.; Weichold, O. UV–vis and IR Spectral Characterization of Persistent Carbenium Ions, Generated upon Incorporation of Cinnamyl Alcohols in the Acid Zeolites HZSM-5 and HMor. *J. Org. Chem.* **2000**, *65* (13), 3947–3951.

(48) Cano, M. L.; Fornés, V.; García, H.; Miranda, M. A.; Pérez-Prieto, J. Characterization of Persistent  $\alpha,\omega$ -Diphenyl Substituted Allyl Cations within Monodirectional Acid Zeolites. *J. Chem. Soc., Chem. Commun.* **1995**, No. 24, 2477–2478.

(49) Humphrey, W.; Dalke, A.; Schulten, K. VMD: Visual Molecular Dynamics. *J. Mol. Graphics* **1996**, *14* (1), 33–38.